

## MIT Open Access Articles

*Chemical Synthesis of Staphyloferrin B Affords Insight into the Molecular Structure, Iron Chelation, and Biological Activity of a Polycarboxylate Siderophore Deployed by the Human Pathogen*

The MIT Faculty has made this article openly available. **Please share** how this access benefits you. Your story matters.

**Citation:** Madsen, Julie L. H., Timothy C. Johnstone, and Elizabeth M. Nolan. "Chemical Synthesis of Staphyloferrin B Affords Insight into the Molecular Structure, Iron Chelation, and Biological Activity of a Polycarboxylate Siderophore Deployed by the Human Pathogen *Staphylococcus Aureus* ." *Journal of the American Chemical Society* 137, no. 28 (July 22, 2015): 9117-9127.

**As Published:** <http://dx.doi.org/10.1021/jacs.5b04557>

**Publisher:** American Chemical Society (ACS)

**Persistent URL:** <http://hdl.handle.net/1721.1/104954>

**Version:** Author's final manuscript: final author's manuscript post peer review, without publisher's formatting or copy editing

**Terms of Use:** Article is made available in accordance with the publisher's policy and may be subject to US copyright law. Please refer to the publisher's site for terms of use.



**Chemical Synthesis of Staphyloferrin B Affords Insight into the Molecular Structure, Iron Chelation, and Biological Activity of a Polycarboxylate Siderophore Deployed by the Human Pathogen *Staphylococcus aureus***

Julie L. H. Madsen,<sup>a</sup> Timothy C. Johnstone<sup>a</sup> and Elizabeth M. Nolan<sup>a,\*</sup>

<sup>a</sup>Department of Chemistry, Massachusetts Institute of Technology, 77 Massachusetts Avenue, Cambridge, MA 02139, USA

\*Corresponding author: [lnolan@mit.edu](mailto:lnolan@mit.edu)

Phone: 617-452-2495

Fax: 617-324-0505

## Abstract

Staphyloferrin B (SB) is a citrate-based polycarboxylate siderophore produced and utilized by the human pathogen *Staphylococcus aureus* for acquiring iron when colonizing the vertebrate host. The first chemical synthesis of SB is reported, which enables further molecular and biological characterization and provides access to structural analogues of the siderophore. SB was prepared in twelve steps from commercially available starting materials with full control of the stereochemistry at the citric acid moiety achieved by using a citric acid synthon containing an alkene moiety. NMR spectroscopic studies confirmed that SB adopts a hemiaminal structure. Addition of synthetic SB to bacterial growth medium recovered the growth of the antibiotic resistant community isolate *S. aureus* USA300 JE2 cultured under conditions of iron limitation. Further, SB-dependent growth recovery required expression of the SB receptor SirA. Two structural analogues of SB, *epi*SB and *SBimide*, were also synthesized and employed to investigate how epimerization of the citric acid moiety or imide formation influence its function as a siderophore. Epimerization of the citric acid stereocenter perturbed the iron-binding properties and siderophore function of SB as evidenced by experimental and computational modeling studies. Although *epi*SB provided growth recovery to *S. aureus* USA300 JE2 cultured in iron-deficient medium, the effect was attenuated relative to that of SB. Moreover, SB more effectively sequestered the Fe(III) bound to human holo-transferrin, an iron source of *S. aureus*, than *epi*SB. *SBimide* is an imide analogous to the imide forms of other citric acid siderophores that are often observed when these molecules are isolated from natural sources. Here, *SBimide* is shown to be unstable, converting to native SB at physiological pH. SB is considered to be a virulence factor of *S. aureus*, a pathogen that poses a particular threat to public health because of the number of drug-resistant strains emerging in hospital and community settings. Iron acquisition by *S. aureus* is important for its ability to colonize the human host and cause disease, and new chemical insights into the structure and function of SB will inform the search for new therapeutic strategies for combating *S. aureus* infections.

## Introduction

The Gram-positive human pathogen *Staphylococcus aureus* is acknowledged as a serious threat to public health because of its ability to subvert the human innate and adaptive immune responses, cause life-threatening disease, and acquire multi-drug resistance.<sup>1-3</sup> Deciphering the numerous strategies that *S. aureus* employs to colonize a host and cause infection at the molecular level is important for developing new therapeutics to treat *S. aureus* infections.<sup>2</sup> Iron is an essential nutrient for almost all organisms,<sup>4-6</sup> and *S. aureus* must acquire this element in the host to colonize and cause infection.<sup>7,8</sup> One strategy that *S. aureus* employs to acquire iron involves the biosynthesis and utilization of siderophores,<sup>9,10</sup> which are small-molecule iron(III) chelators produced by bacteria confronted with conditions of iron limitation.<sup>11-13</sup> Despite significant biological interest in how staphylococcal siderophores contribute to pathogenesis, a paucity of chemical information about these molecules exists. In this work, we combine experimental chemistry, computational modeling, and microbiology to provide the first chemical synthesis and allow structural and functional studies of staphyloferrin B, a polycarboxylate siderophore and virulence factor of *S. aureus*.

Staphyloferrin A (SA) and B (SB) are the two known siderophores produced by *S. aureus*.<sup>9,14</sup> SB was first identified in cultures of *S. aureus* in 1990; however, the isolation was complicated by the instability of the molecule under acidic conditions.<sup>9,14</sup> SB was successfully isolated from culture supernatants of the veterinary pathogen *S. hyicus* DSM 20459 in 1993,<sup>15,16</sup> and was next isolated from culture supernatants of the metal-tolerant Gram-negative soil bacterium *Cupriavidus metallidurans* CH34 (formerly *Ralstonia eutropha* and *Alcaligenes eutrophus*)<sup>17,18</sup> in 1996<sup>18,19</sup> and 1999.<sup>20</sup> *S. aureus* biosynthesizes SB from three building blocks: L-2,3-diaminopropionic acid (L-DAP), citric acid, and  $\alpha$ -ketoglutaric acid ( $\alpha$ KG). Structural determination of SB isolated from *S. hyicus* and *C. metallidurans* resulted in two different structures (Figure 1).<sup>15,20</sup> SB isolated from *S. hyicus* was reported to harbor a linearized  $\alpha$ KG moiety,<sup>15</sup> whereas a cyclic hemiaminal  $\alpha$ KG structure was described for the *C. metallidurans* isolate.<sup>20</sup>

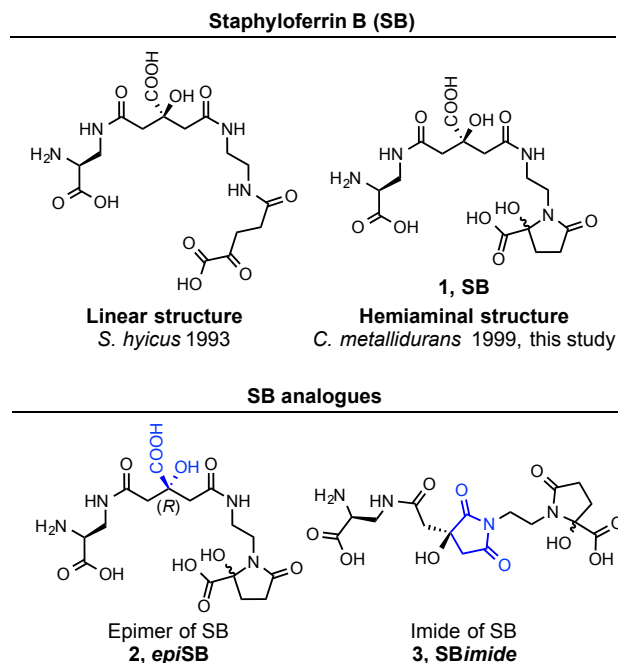


**Figure 1.** Chemical structures and nomenclature of staphyloferrin B (SB, **1**) and two structural analogues. The two structures previously reported for SB are shown.<sup>15,20</sup> SB and the analogues *epiSB* **2** and *SBimide* **3** were prepared and investigated in this work. The structural differences of *epiSB* and *SBimide* compared to native SB are colored in blue.

The linear SB structure contains two stereocenters (C2 and C6, Figure 2) that arise from the DAP and citrate building blocks. The hemiaminal structure contains a third stereocenter at the hemiaminal quaternary carbon atom (C15, Figure 2). Based on feeding studies in which increased production of SB by *S. hyicus* was observed when the culture medium was supplemented with L-DAP but not with D-DAP, the DAP moiety of the siderophore was assigned to have (*S*)-stereochemistry.<sup>15</sup> The assigned (*S*)-stereochemistry of the citric acid moiety was supported by a comparison of the circular dichroism (CD) spectrum of native SB isolated from *C. metallidurans* with the spectra obtained for synthetic DAP-citric acid fragments of SB with either (*R*)- or (*S*)-stereochemistry at the citric acid moiety.<sup>20</sup> The (*S*)-configuration of the citric acid moiety was further supported by the recent crystal structure of SB in complex with its receptor SirA.<sup>21,22</sup> For the hemiaminal structure, the stereocenter of the hemiaminal quaternary

carbon center was reported as a mixture of two isomers in rapid equilibrium *via* the linear SB structure.<sup>20</sup> To date, a structural inconsistency persists in the literature with either the linear or hemiaminal form of SB depicted in different reports, and the linear SB structure is most often shown.

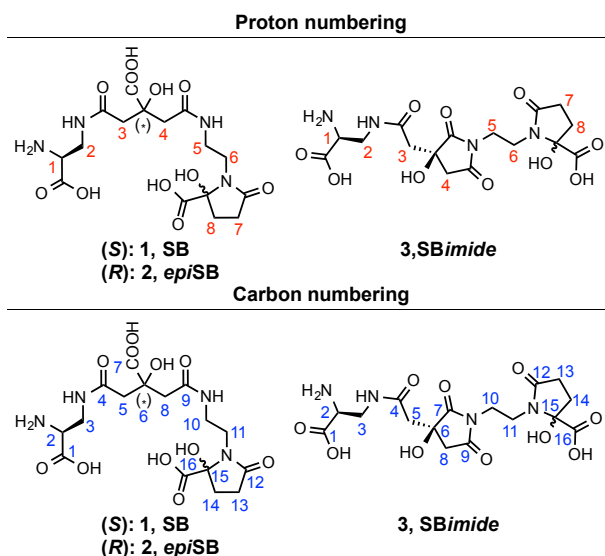


**Figure 2.** Proton and carbon numbering for NMR assignments.

The proteins involved in SB biosynthesis and transport in *S. aureus* have been identified and characterized.<sup>22-30</sup> The *sbn* gene locus (*sbnA-I*) encodes the full biosynthetic machinery (SbnABCEFGH) for the production of SB from the metabolic precursors oxaloacetate, acetyl-coenzyme A, L-glutamate, and O-phospho-L-serine. SbnAB are required for the biosynthesis of L-DAP and  $\alpha$ KG from L-glutamate and O-phospho-L-serine.<sup>26,27</sup> SbnG is an unusual iron-regulated citrate synthase that supplies citrate to the SB biosynthetic pathway by catalyzing an aldol condensation between oxaloacetate and acetyl-CoA.<sup>28</sup> SbnCEF are three non-ribosomal peptide synthetase (NRPS) independent siderophore (NIS)<sup>31</sup> synthetases that work in concert with the decarboxylase SbnH to assemble SB from citrate,  $\alpha$ KG, and two equivalents of L-

DAP.<sup>25</sup> SbnD is an efflux pump that contributes to SB export, and the role of SbnI is as-yet undetermined.<sup>23,30</sup> The enzymes SbnABG enable SB biosynthesis in the absence of the tricarboxylic acid (TCA) cycle,<sup>32</sup> the latter of which is down-regulated by *S. aureus* under conditions of iron limitation.<sup>33</sup> In contrast, the biosynthetic machinery required for SA production, *sfaABCD*, employs citrate produced by the TCA cycle.<sup>32,34</sup> Because *S. aureus* reduces TCA cycle activity in response to the iron-limited environment of the vertebrate host, the differing TCA cycle dependence of SA and SB biosynthesis suggests that SB plays a larger role in *S. aureus* virulence than SA.<sup>32</sup>

A variety of *in vitro* and *in vivo* studies indicate that the SB gene locus contributes to *S. aureus* virulence.<sup>24,34-37</sup> *S. aureus* can enter the bloodstream and cause sepsis, and one set of *in vitro* experiments demonstrated that deletion of the *sbnA-I* gene locus resulted in impaired growth of *S. aureus* strains Newman and RN6390 in horse serum.<sup>34</sup> Moreover, deletion of the NIS synthetase SbnE resulted in impaired growth of *S. aureus* Newman in a mouse kidney abscess model as well as in a rat model of infective endocarditis.<sup>24,37</sup> Transcriptional analysis of *S. aureus* isolates from a rat model of infective endocarditis revealed that the *sbn* locus was up-regulated.<sup>37</sup> In addition to *S. aureus*, some coagulase-negative (CoN) staphylococci biosynthesize SB. A comparison of data obtained from clinical isolates of CoN staphylococci cultured from the peritoneal dialysis fluid of patients showing signs of infection with the data from commensal skin isolates obtained from healthy individuals was performed.<sup>35,36</sup> The CoN staphylococci isolated from the dialysis fluid exhibited higher expression levels of siderophores, particularly SB, than the commensal organisms.<sup>35,36</sup> Taken together, these studies indicate that the *sbn* gene cluster and SB biosynthesis contribute to the pathogenicity of *S. aureus*, and that SB production is linked to the severity of infection at least in animal models. Indeed, strategies to inhibit SB biosynthesis are of interest for therapeutic purposes. Two natural products, baulamycin A and B, isolated from a library of marine microbial-derived natural products were recently identified as inhibitors of SbnE.<sup>38</sup> Further chemical and biological studies addressing

how SB contributes to *S. aureus* virulence and disease progression are needed in light of the public health threat posed by recalcitrant *S. aureus* strains.

In this work, we approach this need from a chemical perspective. We report, to the best of our knowledge, the first total synthesis of SB **1**. This twelve-step synthesis enabled access to two structural analogues, *epi*SB **2** and SB*imide* **3** (Figure 1), as well as chemical and biological evaluation of the resulting siderophores. We address the inconsistent depictions of the SB chemical structure in the literature, confirm that SB is the hemiaminal form, and reevaluate the crystal structure of Fe(III)-SB in complex with its receptor SirA.<sup>21</sup> Moreover, our studies of *epi*SB demonstrate the importance of (*S*)-stereochemistry at the citric acid moiety for the siderophore function of SB. This work provides new chemical insights into this important staphylococcal secondary metabolite and virulence factor, a synthetic platform for the design and preparation of additional SB analogues, and a foundation for future studies at the chemistry/biology interface of how SB contributes to iron homeostasis and microbial pathogenesis.

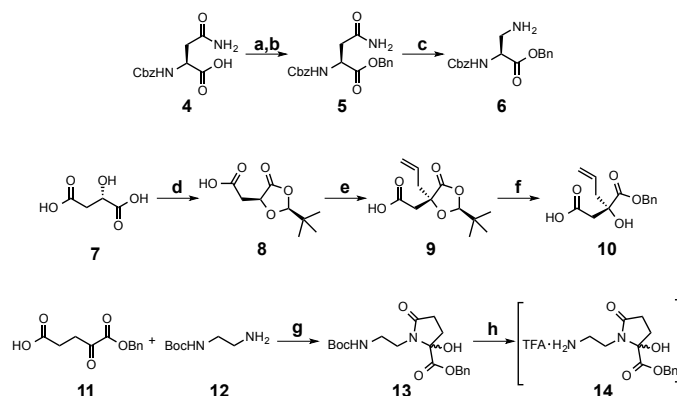
## Results and Discussion

**Chemical Synthesis of Staphyloferrin B and Structural Analogues.** To the best of our knowledge, no total synthesis of SB has been reported, which limits the availability of the native siderophore for investigations of its coordination chemistry, biological activity, role as a virulence factor, and potential in therapeutic design. Structural analogues of SB, which can be readily accessed once a total synthesis has been achieved, are also invaluable in such investigations. In prior structural and functional studies, SB was isolated from bacterial cultures or obtained by *in vitro* reconstitution of the SB biosynthetic pathway.<sup>15,16,20,25</sup> An unresolved issue concerns the chemical structure of SB, which has been inconsistently presented in the literature (Figure 1). To enable further physicochemical and biological studies of SB, gain synthetic access to structural analogues of the siderophore, and address the structural discrepancy, we designed and executed a total synthesis that affords native SB (Scheme 1). The synthesis was achieved in twelve steps from four commercially available starting materials:

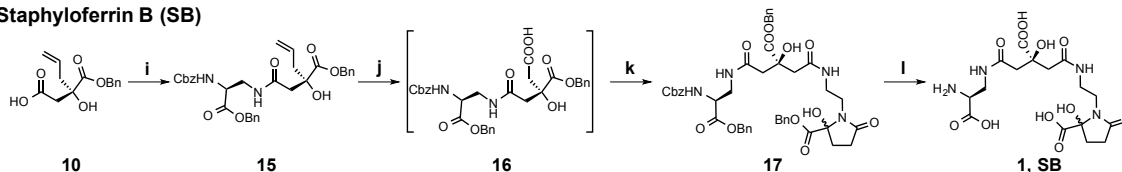
(S)-malic acid, Z-L-asparagine, 1,2-diaminoethane (DAE) and  $\alpha$ KG. The major challenges posed by the synthesis were control of the stereogenic center of the citric acid moiety and control/prevention of imide formation by the citric acid moiety during the reactions and purification steps (Supporting Information).

The synthesis is based on three building blocks, **6**, **10**, and **14**. Cbz- and benzyl-protected L-DAP **6** was prepared in two steps from Z-L-asparagine by initial benzyl protection of the carboxylic acid followed by a Hofmann rearrangement to generate the primary amine **6**. Coupling of *N*-boc-diaminoethane **12** to mono-benzylated  $\alpha$ -ketoglutarate **11**, the latter of which was prepared according to a procedure in the patent literature,<sup>39</sup> afforded the hemiaminal product **13**. The cyclic hemiaminal structure of **13** was confirmed by HSQC and HMBC 2D NMR spectroscopy, which revealed a correlation between the internal methylene protons 4 of the diaminoethane moiety to both the quaternary stereocenter 9 and the carbonyl carbon 6 of the hemiaminal ring (Figure S1). The carbamate protecting group of hemiaminal **13** was removed by using trifluoroacetic acid (TFA) in dichloromethane to yield amine **14**. In order to control the stereochemistry of the citric acid moiety throughout the synthesis, a citric acid synthon **10** was employed. Masking one of the enantiotopic carboxylic acids of citric acid as an alkene afforded full control of the stereochemistry. Starting from (S)-malic acid, reaction with trimethylacetaldehyde afforded dioxolanone **8** stereoselectively.<sup>40</sup> Allylation of the dioxolanone using lithium hexamethyldisilazide (LiHMDS) as the base provided alkene **9**, which was ring-opened in a transesterification reaction to afford benzyl ester **10**.<sup>41</sup> Intermediates **6**, **10**, and **14** were subsequently employed as building blocks for the assembly of SB and the structural analogues.

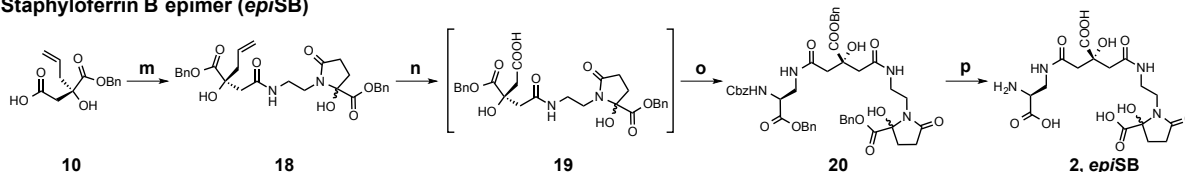
### Building blocks



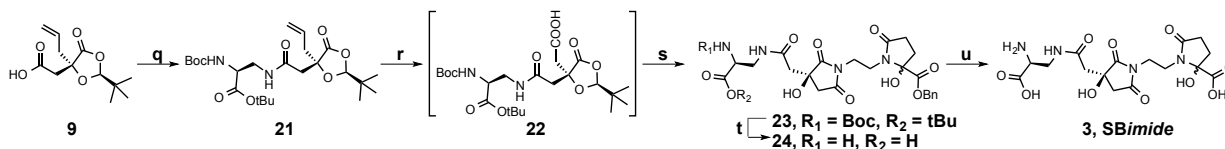
### Staphyloferrin B (SB)



### Staphyloferrin B epimer (*epi*SB)



### Staphyloferrin B imide (SBimide)



(a) Cs<sub>2</sub>CO<sub>3</sub>, H<sub>2</sub>O, MeOH; (b) BnBr, DMF, 76% yield over two steps; (c) PhI(OAc)<sub>2</sub>, pyridine, DMF, H<sub>2</sub>O, 50% yield; (d) Trimethylacetaldehyde, *p*-TsOH, H<sub>2</sub>SO<sub>4</sub>, pentane, 42 °C, 40% yield; (e) Allyl bromide, LHMDS, THF, -78°C, 51% yield; (f) BnOH, NaH, 0 °C, 98% yield; (g) EDC, HOAt, DIPEA, CH<sub>2</sub>Cl<sub>2</sub>, 60% yield; (h) 33% TFA in CH<sub>2</sub>Cl<sub>2</sub>, 0 °C, quant. yield; (i) **6**, HATU, HOAt, DIPEA, CH<sub>2</sub>Cl<sub>2</sub>, 69% yield; (j) NaIO<sub>4</sub>, RuCl<sub>3</sub>, MeCN, H<sub>2</sub>O, 89% yield; (k) **14**, HATU, HOAt, DIPEA, CH<sub>2</sub>Cl<sub>2</sub>, 43% yield; (l) Pd(OH)<sub>2</sub>/C, H<sub>2</sub>, MeOH, 87% yield; (m) **14**, HATU, HOAt, DIPEA, CH<sub>2</sub>Cl<sub>2</sub>, 72% yield; (n) NaIO<sub>4</sub>, RuCl<sub>3</sub>, MeCN, H<sub>2</sub>O, 86% yield; (o) **6**, HATU, HOAt, DIPEA, CH<sub>2</sub>Cl<sub>2</sub>, 38% yield; (p) Pd(OH)<sub>2</sub>/C, H<sub>2</sub>, MeOH, 93% yield; (q) Boc-DAP-O*t*Bu, HATU, HOAt, DIPEA, CH<sub>2</sub>Cl<sub>2</sub>, 75% yield; (r) NaIO<sub>4</sub>, RuCl<sub>3</sub>, EtOAc, MeCN, H<sub>2</sub>O, 89% yield; (s) **14**, EDC, HOAt, NMM, CH<sub>2</sub>Cl<sub>2</sub>, 45% yield; (t) 10% H<sub>2</sub>O, 45% TFA, 45% CH<sub>2</sub>Cl<sub>2</sub>, 4 °C, 66% yield; (u) Pd(OH)<sub>2</sub>/C, H<sub>2</sub>, MeOH, 86% yield.

### Scheme 1. Syntheses of SB **1**, *epi*SB **2**, and SBimide **3**.

SB was prepared in four steps beginning with the coupling of synthon **10** to Z-DAP-OBn **6** in a 30-min amide coupling reaction that employed HATU/HOAt as coupling reagents. The resulting alkene **15** was oxidized to the corresponding carboxylic acid with *in situ*-generated perruthenate as the oxidant,<sup>42</sup> and the corresponding carboxylic acid **16** was employed directly

in an amide coupling reaction with the hemiaminal building block **14**, affording fully protected SB **17**. The product was obtained as a mixture of stereoisomers as a result of the equilibrating hemiaminal quaternary carbon. This mixture of isomers was also reported for SB that was isolated from natural sources.<sup>20</sup> In the final step, the siderophore was globally deprotected in a hydrogenation reaction, which provided SB **1** with an overall yield of 22% for these four steps.

The epimeric analogue of SB, *epi*SB **2**, differs from SB only in the stereochemistry of the citric acid moiety where it possesses (*R*)-stereochemistry. This analogue was synthesized using the same building blocks employed for SB and simply reversing the order of the coupling reactions. By coupling the citric acid synthon **10** to hemiaminal **14** prior to oxidation of the alkene, the stereochemistry of the citric acid moiety in the resulting siderophore product was inverted. Following the same reaction procedures described for SB, *epi*SB **2** was also obtained in an overall yield of 22% for these four steps.

The imide analogue of SB, *SBimide* **3**, differs from SB by having the carboxylic acid of the citric acid moiety closed in an imide ring with the neighboring amide nitrogen of the DAE moiety. A different synthetic strategy was employed to obtain *SBimide* in a regioselective manner. Two regioisomers of the imide can be formed, and both isomers were observed as byproducts during preliminary studies of the total synthesis of SB when no precautions were taken to prevent this side reaction (see Supporting Information for further discussion). *SBimide* was prepared regioselectively where only the DAE amide nitrogen participates in imide formation (Scheme 1). Dioxolanone **9** was found to promote imide formation during amide couplings of extended reaction time when applied as the citric acid synthon. Thus, to afford **21** without imide formation, amide coupling between commercially available Boc-DAP-OtBu and dioxolanone **9** was performed using HATU/HOAt for 30 min. Following oxidation of alkene **21** to afford carboxylic acid **22**, this intermediate was allowed to react with hemiaminal **14** in a second amide coupling using EDC/HOAt as coupling reagents. The coupling reaction time was extended to 20 h, providing the DAE-closed imide **23** as the major product. Following

purification and global deprotection, *SBimide* **3** was obtained in an overall yield of 17% for these five steps.

**SB Displays a Cyclic Hemiaminal Structure.** The reported chemical structure of SB is inconsistent throughout the literature (Figure 1). In 1993, a chemical structure of SB containing a linear  $\alpha$ KG moiety was reported.<sup>15</sup> The  $^{13}\text{C}$  NMR spectroscopic data presented in this early study revealed that the chemical shift of one carbonyl carbon atom was shifted from the expected  $\approx 200$  ppm to 91 ppm. This change in chemical shift was rationalized by hydration of the corresponding ketone. In 1999, a structure of SB containing a cyclic hemiaminal  $\alpha$ KG moiety was reported.<sup>20</sup> This study presented a  $^{13}\text{C}$  NMR spectrum that exhibited a resonance with a chemical shift of 94 ppm. This peak was shown by 2D NMR to arise from hemiaminal formation of the  $\alpha$ KG moiety, resulting in a quaternary carbon center. Although the correct structure of SB seems to be the hemiaminal structure on the basis of the 2D NMR analysis and the similar  $^{13}\text{C}$  NMR spectra obtained for the two isolates, the linear structure of SB is more frequently depicted in the literature. To help clarify this matter, we studied synthetic SB by NMR spectroscopy and compared these data to those obtained for SB isolated from natural sources (Table S3 and S4). The observed chemical shifts of all proton and carbon atoms of synthetic SB correspond well with the reported data,<sup>15,20</sup> and minor differences can be attributed to the different spectroscopic conditions. We employed HMBC 2D NMR spectroscopy to identify long-range correlations in the molecule. Clear correlations between methylene protons 6 of the DAE moiety and both the hemiaminal ring quaternary carbon 15 and carbonyl carbon 12 were observed, confirming that the structure of SB in aqueous solution contains the cyclic hemiaminal (Figures 2, S2).

The NMR spectra of *epi*SB are very similar to those of SB (Table S3 and S4, Figure S3). A comparison of the spectra of SB to those of *SBimide* reveals a clear difference for the methylene protons 3 and 4 of the citric acid moiety (Figure 2, Table S3). For SB, these four protons produce four distinct doublets, whereas the same proton signals of *SBimide* overlap and result in two doublets and one multiplet signal. In addition, the HMBC spectrum of *SBimide* showed correlations between the two carbonyl carbons 7 and 9 of the imide ring and the

neighboring methylene protons 5 of the DAE moiety, making the distinction of the two compounds unambiguous (Figures 2,S4).

**Re-Evaluation of a Crystal Structure of Fe(III)-SB Bound to SirA.** The hemiaminal structure of SB reported in 1999 is largely forgotten in the siderophore and *S. aureus* literature for reasons that are unclear. Recently, a crystal structure of Fe(III)-SB in complex with SirA, the SB receptor of *S. aureus*, was reported with the linear structure of Fe(III)-SB modeled into the binding site (PDB 3MWF).<sup>21</sup> In this structural determination, the electron density of the siderophore backbone spanning the citrate, DAE, and  $\alpha$ KG moieties is not well defined, as noted in the original report.<sup>21</sup> Our confirmation of the hemiaminal structure of SB in aqueous solution motivated us to investigate the electron density map of Fe(III)-SB-SirA and determine whether the hemiaminal form provides a better fit to the electron density corresponding to the bound siderophore. In order to perform this analysis, we determined the lowest energy structure of Fe(III)-SB to be  $\Lambda$ -Fe(III)-SB(SSR) (*vide infra*, Table S5, Figure S5) by computational methods; a comparison of the corresponding calculated CD spectrum with that obtained experimentally for Fe(III)-SB provided support for the validity of the computational result. When we aligned the computationally optimized  $\Lambda$ -Fe(III)-SB(SSR) hemiaminal structure with the linear structure reported in the crystal structure of Fe(III)-SB-SirA, we found that the structures of the iron complexes differ significantly only in the vicinity of the DAE and  $\alpha$ KG units (Figure 3). Further analysis of the electron density in the area where the hemiaminal and linear structures differ indicates that the hemiaminal form of SB provides a better fit to the electron density than the linear structure (Figure 3). This analysis reveals that the hemiaminal Fe(III)-SB structure, not the linear structure, is bound to SirA in the crystal structure, and provides further support for the conclusion that the hemiaminal is the form of SB isolated from *S. aureus* cultures.

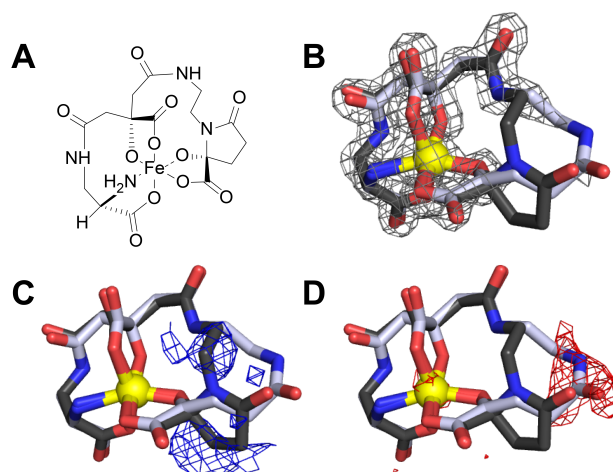


**Figure 3.** Overlay of the calculated Fe(III)-SB structure based on the hemiaminal form (dark grey carbon sticks) and the crystallographically determined Fe(III)-SB (light grey carbon sticks). (A) Chemical structure of Fe(III)-SB. (B) The  $F_o$  map, contoured at  $2\sigma$  and  $1.6 \text{ \AA}$  from the atoms modeled into the electron density, is shown as a grey mesh. The  $2F_o - F_c$  map, contoured at  $3\sigma$  showing (C) positive electron density as a blue mesh and (D) negative electron density as a red mesh. Color code: C: light or dark grey, O: red, N: blue, and Fe: yellow sphere.

**Fe(III)-Binding Properties and Photochemistry of SB.** SB chelates Fe(III) in a hexadentate manner, utilizing the two  $\alpha$ -hydroxy carboxylic acids and the  $\alpha$ -amino carboxylic acid as three bidentate ligands (Figure 3). This coordination mode is supported by both the crystal structure of Fe(III)-SB bound to SirA<sup>21</sup> and an NMR study of Ga(III)-SB.<sup>20,21</sup> Solution studies of Fe(III) chelation by SB are limited, however. Elucidating the Fe(III)-binding properties of SB in solution is essential for achieving a thorough understanding of the role of SB in iron homeostasis and as a virulence factor of *S. aureus* as well as informing experimental design for studies that utilize the Fe(III)-SB complex. We therefore employed synthetic SB to examine the Fe(III) coordination complex. In agreement with previous reports, addition of Fe(III) to SB resulted in formation of a charge-transfer band centered at  $\approx 330 \text{ nm}$  (Figure 4A).<sup>15,16</sup> Moreover, the CD spectrum of Fe(III)-SB revealed a positive Cotton effect at the wavelengths of the charge-transfer band, which is also in agreement with the CD spectrum of Fe(III)-SB isolated from *S. hyicus* cultures (Figure 4B).<sup>15</sup>

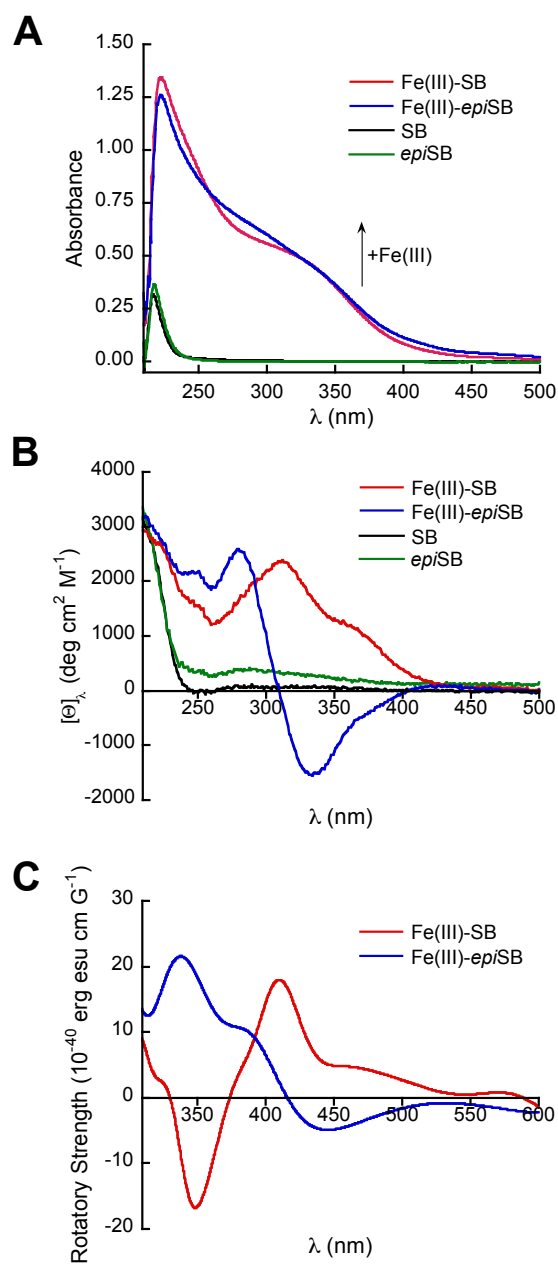


**Figure 4.** Iron-binding studies of SB and *epi*SB. (A) Optical absorption spectrum of 200  $\mu$ M apo and Fe(III)-bound siderophores in 10 mM HEPES, 100 mM KCl, pH 7.4. (B) CD spectra of 300  $\mu$ M apo- and Fe(III)-bound siderophores in Milli-Q water. (C) Theoretical CD spectra of  $\Lambda$ -Fe(III)-SB(*SSR*) and  $\Delta$ -Fe(III)-*epi*SB(*SRS*) as determined by TD-DFT calculations. SB (black), *epi*SB (green), Fe(III)-SB (red), and Fe(III)-*epi*SB (blue).

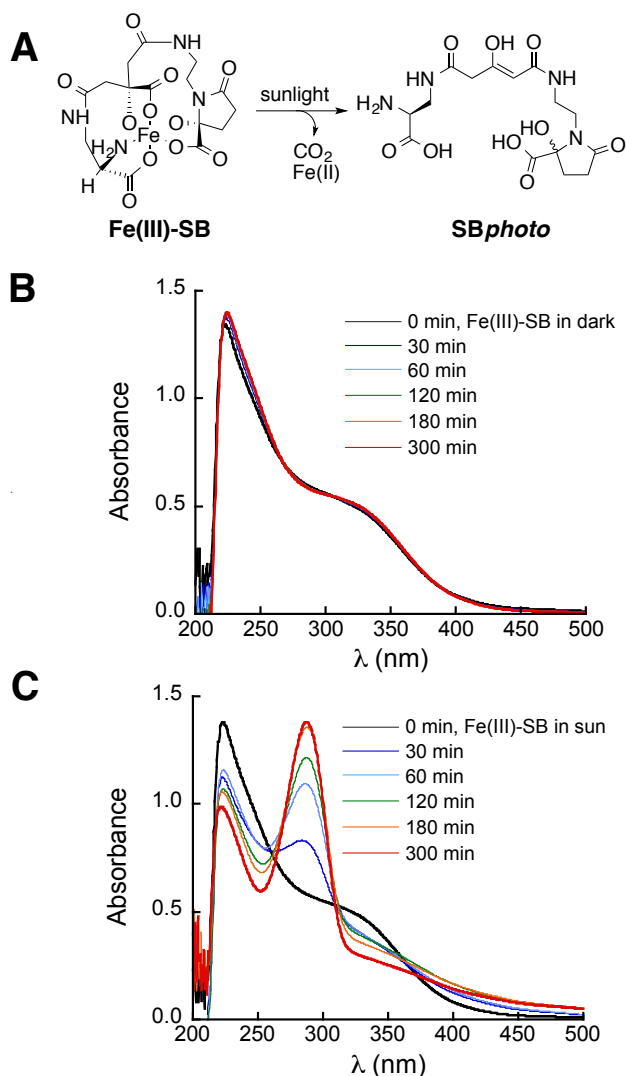


**Figure 5.** Photoreactivity of Fe(III)-SB. (A) Photoreaction of Fe(III)-SB. (B) Optical absorption spectra for Fe(III)-SB incubated in the dark. (C) Optical absorption spectra for Fe(III)-SB exposed to sunlight for the indicated times. The photoreactions were performed with 200  $\mu$ M Fe(III)-SB in 10 mM HEPES, 100 mM KCl, pH 7.5, rt.

Because Fe(III) complexes of citric acid siderophores, including those of petrobactin<sup>43</sup> and aerobactin,<sup>44</sup> undergo photochemistry when exposed to sunlight, we questioned whether Fe(III)-SB exhibits similar photochemistry. The photoreaction of these siderophores involves decarboxylation of the carboxylic acid at the citric acid moiety, followed by oxidation of the resulting secondary alcohol to generate a  $\beta$ -hydroxy- $\alpha,\beta$ -unsaturated amide, and the Fe(III) is concomitantly reduced to Fe(II) (Figure 5A).<sup>43,44</sup> The optical absorption spectrum of Fe(III)-SB in

aqueous solution remained unchanged when the complex was incubated in the dark (Figure 5B). In contrast, when we exposed an aqueous solution of Fe(III)-SB to sunlight and recorded the optical absorption spectrum at various time points, formation of a new absorbance feature centered at 290 nm occurred over the course of 3 h (Figure 5C), revealing that Fe(III)-SB is photoreactive. This absorbance feature is in agreement with previous reports of photoproducts from structurally related siderophores.<sup>43,44</sup> Light was therefore excluded during all chemical and biological experiments with the Fe(III)-siderophore complexes.

**Epimerization of the Citric Acid Stereocenter Perturbs the Fe(III)-binding Properties of SB.** During some exploratory experiments with SB and its structural analogues, we performed a chrome azurol S agar diffusion (CASAD) assay.<sup>45</sup> The chrome azurol S (CAS) assay provides colorimetric detection of apo siderophores and is routinely used to screen for the presence of siderophores in bacterial culture supernatants.<sup>46</sup> Siderophore detection is based on the ability of siderophores to sequester Fe(III) from the indicator formed from CAS, hexadecyltrimethylammonium (HDTMA) bromide, and Fe(III). Siderophore sequestration of Fe(III) from the CAS results in a color change from blue to orange. When performed using agar diffusion plates (CASAD assay), siderophores can be detected based on the radius and color of the orange disks formed following addition of a solution containing siderophores to the plate. The “siderophore activity” is qualitatively assayed by the color intensity and size of the orange disks. Siderophores that coordinate Fe(III) with relatively high affinity will afford brighter orange disks relative to siderophores that bind Fe(III) with relatively low affinity. Moreover, higher siderophore concentrations will result in larger disks because more siderophores diffuse in the plate. When we spotted SB on CASAD plates, we observed orange spots that indicated sequestration of Fe(III) from the indicator and, as expected, the radius of the spots increased with increasing the concentration of SB (Figure 6). A comparison of the spots obtained for equimolar quantities of SB and *epi*SB indicated that *epi*SB coordinates Fe(III) with lower affinity than SB. Less orange color evolved for the *epi*SB spots relative to those for SB. This qualitative,

colorimetric assay provided the first evidence that epimerization of the citric acid stereocenter perturbs the Fe(III)-binding properties of SB.

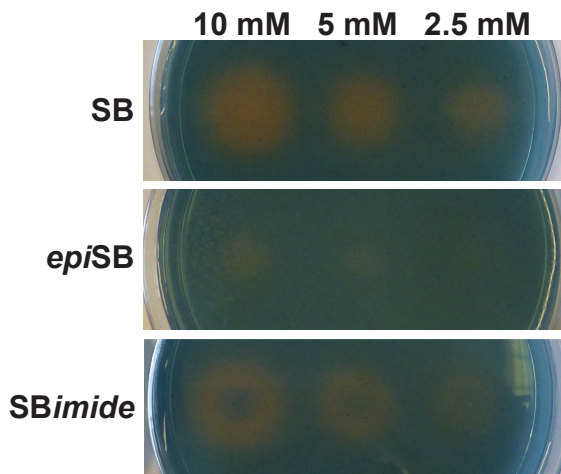


**Figure 6.** Chrome azurol S agar diffusion (CASAD) assay comparing Fe(III) scavenging by SB, *epiSB*, and *SBimide*. The agar plate was spotted with each siderophore at concentrations of 2.5, 5, and 10 mM (10  $\mu$ L/spot).

Similarly to Fe(III)-SB, the optical absorption spectrum of Fe(III)-*epiSB* exhibits a charge-transfer band centered at  $\approx 330$  nm (Figure 4A). An overlay of the optical absorption spectra of Fe(III)-SB and Fe(III)-*epiSB* reveals subtle differences, which suggests that the Fe(III) coordination sphere is perturbed by epimerization of the citric acid moiety. As expected, the CD spectrum of Fe(III)-*epiSB* differs from that of SB. The molar ellipticity of the Fe(III)-*epiSB* complex shifts from positive to negative across the 275-400 nm region of the spectrum and the intercept of the Fe(III)-*epiSB* spectrum with the abscissa coincides with the wavelength of maximum molar ellipticity (315 nm) of the Fe(III)-SB complex (Figure 4B).

To obtain more quantitative insight into how epimerization of the citric acid stereocenter perturbs the Fe(III)-binding properties of SB, we determined  $p\text{Fe(III)}$  values for SB and *epiSB*. The  $p\text{Fe(III)}$  is defined as the negative logarithm of the unbound iron concentration in the presence of 10  $\mu$ M ligand and 1  $\mu$ M Fe(III) at pH 7.4.<sup>47</sup> This value is commonly used to compare

the Fe(III) affinities of siderophores. We performed EDTA competition titrations where the Fe(III)/EDTA/siderophore mixtures were incubated for 16 h at room temperature prior to analysis, and determined the pFe(III) values of SB and *epi*SB to be 23.6 and 23.2, respectively, at this time point (Figure S8). These pFe(III) values are similar to the experimentally determined pFe(III) values of other citric acid siderophores including petrobactin (pFe = 23.0)<sup>48</sup> and aerobactin (pFe = 23.3)<sup>47</sup> (Table S7). Moreover, the relative pFe(III) values of SB and *epi*SB are in agreement with the CASAD assay results and indicate that *epi*SB coordinates Fe(III) with lower affinity than native SB. One caveat to these pFe(III) experiments and the data interpretation involves the equilibration time. Literature procedures for pFe(III) determination typically describe incubation times of 16-24 h, and these protocols provided a basis for our initial experimental design.<sup>48-50</sup> We attempted to determine pFe(III) values at time points >16 h to probe whether a longer incubation period is required for equilibrium to be achieved; however, these experiments were compromised because of decomposition of SB/Fe(III)-SB as evidenced by subtle changes in the optical absorption spectra of Fe(III)-SB over time (up to seven days). Thus, whether the measurements were performed using samples that had reached equilibrium is unclear.

**Computational Modeling Provides Further Insight into the Fe(III)-SB Coordination Sphere.** To gain further insight into the consequences of epimerization of the citric acid stereocenter on Fe(III) chelation, we investigated the structures of Fe(III)-SB and Fe(III)-*epi*SB using computational methods. The six donor atoms of SB and *epi*SB are chemically distinct, affording an M(ABCDEF) system that can occur as 30 different geometric isomers. The majority of these possible structures are not relevant because of steric constraints imposed by the ligand. Because SB is composed of three bidentate ligands, the skew-lines convention ( $\Delta/\Lambda$ ) can be used to describe the helicity at the metal center.<sup>51</sup> Four isomers were constructed manually for each Fe(III)-SB and Fe(III)-*epi*SB isomer spanning the combinations allowed by  $\Delta$  or  $\Lambda$  helicity and *R* or *S* chirality at the quaternary hemiaminal carbon center 15 (Figure 2). The conformations of these hand-built structures were first subjected to a semi-empirical

conformational search to determine the energetically feasible conformations. Subsequent density functional theory (DFT) calculations revealed that the lowest energy Fe(III)-SB structure ( $-2946.206 E_h$ ) was  $\Lambda$ -Fe(III)-SB(SSR). The notation used indicates that in this species the Fe(III) is chelated with  $\Lambda$  helicity and the stereochemical descriptors in parentheses provide the chirality at the DAP (carbon 2), citrate (carbon 6), and hemiaminal (carbon 15) stereocenters. (Figure S5). The  $\Delta$ -Fe(III)-SB(SSS) isomer was found to be of higher energy ( $-2946.181 E_h$ ), whereas the configurations of  $\Lambda$ -Fe(III)-SB(SSS) and  $\Delta$ -Fe(III)-SB(SSR) converted to the opposite helicity during the DFT geometry optimization (Table S5). The lowest energy structure for the Fe(III)-*epi*SB complex,  $\Delta$ -Fe(III)-*epi*SB(SRS) ( $-2946.198 E_h$ ), has the opposite ligand helicity and quaternary carbon center chirality compared to the lowest energy structure of native Fe(III)-SB (Figure S5). The energies of the less stable conformations are listed in Table S5. Next, we employed time-dependent DFT (TD-DFT) to simulate CD spectra corresponding to the lowest energy structures,  $\Lambda$ -Fe(III)-SB(SSR) and  $\Delta$ -Fe(III)-*epi*SB(SRS), and compared these predictions to the experimentally obtained spectra (Figure 3B,C). In agreement with the experimental data, the calculated spectra exhibited a positive Cotton effect for  $\Lambda$ -Fe(III)-SB(SSR) and a shift from positive to negative for  $\Delta$ -Fe(III)-*epi*SB(SRS) in the low energy spectral feature, thereby supporting the different coordination geometries of the two lowest energy complexes.

The geometry optimizations allowed further investigation of the Fe(III) coordination spheres of SB and *epi*SB. The two most regular coordination geometries of six-coordinate metal complexes are octahedral and trigonal prismatic. The twist angle,  $\alpha$ , defined as the angle formed between two opposite metal-ligand bonds when viewing the complex along the  $C_3$ -axis, can be used to distinguish these coordination modes (Figure S6B).<sup>52</sup> With this definition, idealized octahedral complexes have  $\alpha = 60^\circ$  and trigonal prismatic complexes have  $\alpha = 0^\circ$ . Upon inspection of the coordination polyhedron of Fe(III)-SB (Figure S6A),<sup>53</sup> it can be appreciated that the geometry is distorted from octahedral. When viewed along the pseudo  $C_3$ -symmetry axis, it becomes apparent that the  $\alpha$  values are intermediate between those of the

octahedron and the trigonal prism (Figure S6B). The average of twist angles  $\alpha_i$ ,  $\alpha_{ii}$ , and  $\alpha_{iii}$  for  $\Delta$ -Fe(III)-SB(SSR) is  $36^\circ$ , indicating a significant distortion towards trigonal prismatic. The average twist angle for the  $\Delta$ -Fe(III)-*epi*SB(SRS) structure is  $-29^\circ$ , reflecting a similar trigonal prismatic distortion of the two complexes with opposite helicity at the metal center.

**Epimerization of the Citric Acid Stereocenter Perturbs the Siderophore Activity of SB.** We employed a *S. aureus* growth recovery assay to evaluate the siderophore activity, which we define as the ability of a siderophore to recover bacterial growth under conditions of iron limitation, of SB, *epi*SB, and SB*imide*. For this assay, we obtained two mutant strains, hereafter  $\Delta$ *sbnE* and  $\Delta$ *sirA*, of the multi-drug resistant community isolate *S. aureus* USA300 JE2 from the Nebraska Transposon Mutant Library (NTML).<sup>54</sup> The siderophore-deficient  $\Delta$ *sbnE* mutant cannot biosynthesize SB because it lacks SbnE, the first NIS synthetase in the SB biosynthetic pathway encoded by the SB gene locus. This mutant is a useful tool for studying the effect of exogenous SB and its structural analogues on *S. aureus* growth because there will be no competition resulting from production of the endogenous siderophore. The  $\Delta$ *sirA* mutant is deficient in the membrane receptor SirA responsible for Fe(III)-SB uptake and therefore cannot import SB (Table S1).<sup>22</sup> The mutant strains were identified using the NTML gene explorer (see further description in Supporting Information). The strains were cultured under either iron-sufficient or -deficient conditions. A defined minimal medium, Tris-minimal succinate (TMS) medium, was employed for all studies, and the medium was supplemented with the chelator 2,2'-dipyridyl (200  $\mu$ M, DP) to mimic conditions of iron limitation. When cultured in 96-well plates and in the absence of DP, both  $\Delta$ *sbnE* and  $\Delta$ *sirA* grew to an OD<sub>600</sub> of  $\approx 0.6$  following a 10-h incubation at 37 °C. The growth of both strains was impaired when DP was included in the TMS medium. Under such iron-deficient conditions, an OD<sub>600</sub> of  $\approx 0.2$  was observed following the 10-h incubation period (Figure 7 and S9).

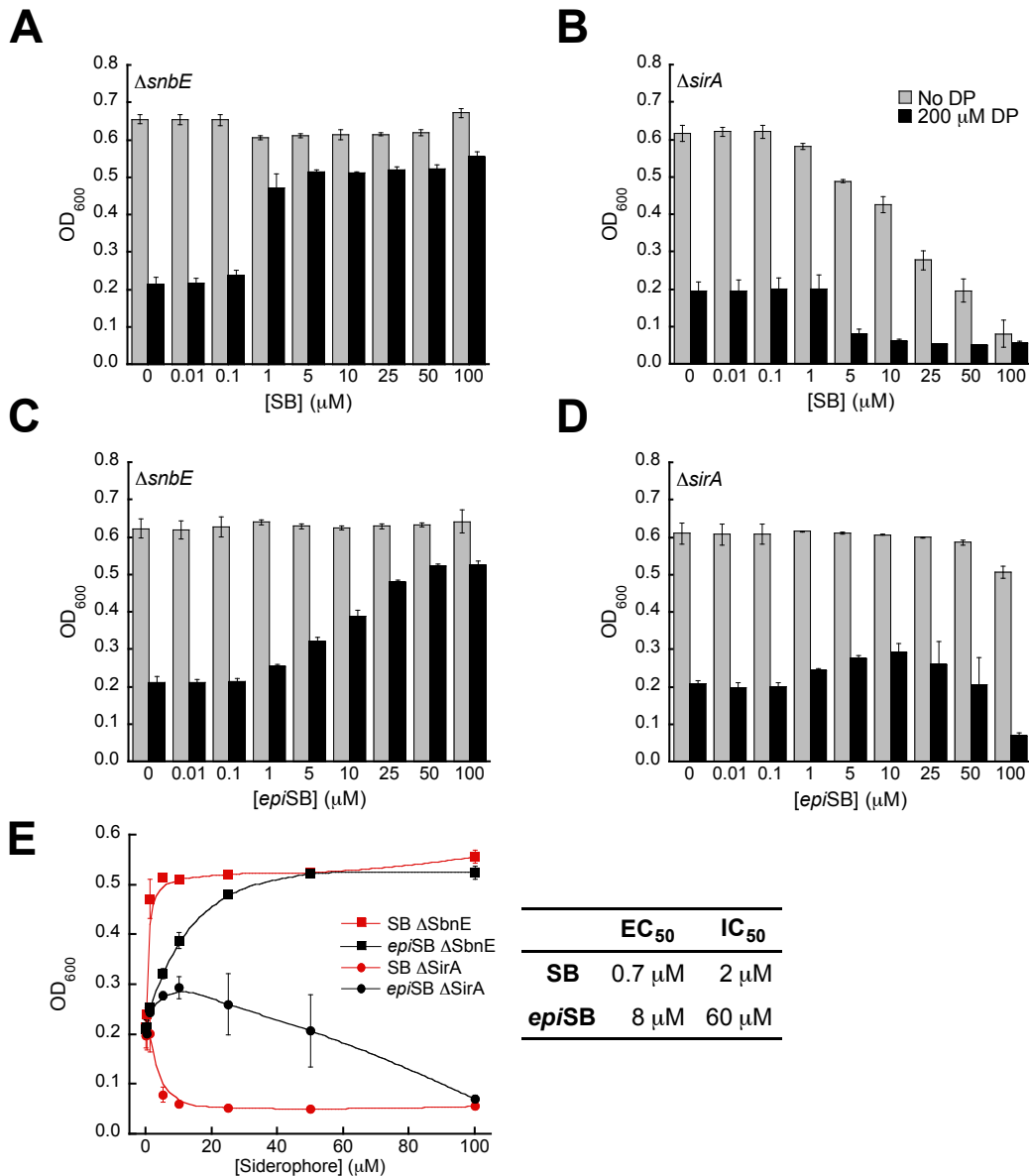


**Figure 7.** Growth recovery assays of the  $\Delta sbnE$  and  $\Delta sirA$  mutants of *S. aureus* in the presence of increasing concentration of SB or *epiSB* in the growth medium (37 °C, t = 10 h). Iron sufficient conditions, TMS medium (gray), Iron deficient conditions, TMS medium + 200  $\mu\text{M}$  DP (black). (A) SB-mediated growth recovery of *S. aureus*  $\Delta sbnE$ ; (B) Growth inhibition by SB of *S. aureus*  $\Delta sirA$ ; (C) *epiSB*-mediated growth recovery of *S. aureus*  $\Delta sbnE$ ; (D) Growth inhibition by *epiSB* of *S. aureus*  $\Delta sirA$ . (E) The OD<sub>600</sub> at t = 10 h plotted as a function of siderophore concentration and tabulated IC<sub>50</sub> and EC<sub>50</sub> values determined from the plot. The results are the average of three independent trials, error bars are standard deviations. The growth recovery assay was monitored for 22 h and the full growth curve plots are shown in Figure S9.

In the absence of DP, addition of SB to the culture medium had negligible effect on the growth of the  $\Delta sbnE$  mutant as ascertained by OD<sub>600</sub> values. Under iron-deficient conditions where the growth of  $\Delta sbnE$  is impaired, SB afforded growth recovery of the strain in a concentration-dependent manner. The OD<sub>600</sub> of the cultures increased to  $\approx 0.5$  when  $>1 \mu\text{M}$  SB was added to the TMS medium containing DP; however, full growth recovery of  $\Delta sbnE$  was not observed under these conditions (Figure 7A). Inductively coupled plasma mass spectrometry established that the TMS medium contains 700 nM of total iron (Table S2). Thus, maximum growth recovery occurred when the concentration of SB equaled or exceeded the concentration of total Fe in the medium. To determine whether Fe(III)-SB can fully recover the growth of  $\Delta sbnE$ , we performed an experiment where SB was preloaded with Fe(III) prior to the assay, and observed that the Fe(III)-SB complex ( $10 \mu\text{M}$ ) afforded full growth recovery of  $\Delta sbnE$  (Figure S10).

The  $\Delta sirA$  mutant lacks the SB receptor and cannot import Fe(III)-SB.<sup>22</sup> Addition of apo SB ( $>1 \mu\text{M}$ ) to cultures of  $\Delta sirA$  resulted in growth inhibition regardless of the absence or presence of DP in the medium (Figure 6B). The inhibited growth of  $\Delta sirA$  can be attributed to sequestration of iron in the growth medium by SB, which persists as a high-affinity extracellular iron chelator because it cannot be imported by the  $\Delta sirA$  mutant. Taken together with the data for  $\Delta sbnE$ , these growth recovery assays confirm that synthetic SB exhibits siderophore activity and delivers iron to *S. aureus*. Moreover, the siderophore activity depends on iron availability and requires the membrane receptor SirA.

Next, the growth recovery assay was performed using *epiSB* to evaluate the importance of the stereochemistry of the citric acid moiety for siderophore activity. The results indicate that *epiSB* possesses siderophore activity that is dependent on the SB receptor SirA (Figure 7C,D). Thus, the (*S*)-stereochemistry at the citric acid moiety of SB is not essential for *S. aureus* to use this siderophore for acquiring iron. Nevertheless, *epiSB* exhibits reduced siderophore activity compared to SB. Under conditions of iron limitation, *epiSB* recovers the growth of the  $\Delta sbnE$  mutant, but maximum growth recovery is observed at  $50 \mu\text{M}$  *epiSB*, whereas the cultures

recover to a similar OD<sub>600</sub> value with 1 μM SB (Figure 7A,C). Moreover, higher concentrations of *epi*SB relative to SB are required to inhibit growth of the  $\Delta$ *sirA* mutant (Figure 7B,D). The difference in siderophore activity between the two analogues was quantified by comparing EC<sub>50</sub> (concentration resulting in 50% growth recovery of  $\Delta$ *sbnE*) as well as IC<sub>50</sub> (concentration resulting in 50% growth inhibition of  $\Delta$ *sirA*) values obtained from the growth recovery assay data (Figure 7E). The EC<sub>50</sub> and IC<sub>50</sub> values of SB are 10-fold and 30-fold lower, respectively, than the values obtained for *epi*SB. The reduced siderophore activity of *epi*SB may result from its lower Fe(III) affinity, as indicated by the CASAD assay and pFe(III) value determination. Indeed, the reduced IC<sub>50</sub> value of *epi*SB against  $\Delta$ *sirA* supports this notion. Nevertheless, it is also possible that epimerization of the citric acid moiety impairs recognition and/or transport of the ferric complex by SirA. An investigation of vibrioferrin diastereoisomers differing only in the stereochemistry of the citric acid moiety revealed that only the natural (*R*)-isomer possesses siderophore activity,<sup>55</sup> which is in contrast to the observed siderophore activity of *epi*SB. On the basis of the published work, it is unclear whether the impaired siderophore activity of *epi*-vibrioferrin results from impaired Fe(III)-binding properties or because the membrane receptor cannot recognize and/or transport the non-native epimer.<sup>55</sup>

**SBimide Converts to SB Under Simulated Physiological Conditions.** We also examined whether SBimide (Figure 1) is able to chelate Fe(III) and influence the growth of *S. aureus*. Imide byproducts of citric acid siderophores are commonly observed when these siderophores are isolated from natural sources.<sup>14</sup> During the course of this work, we observed imide byproducts during optimization of the total synthesis of SB (Supporting Information). As a result, we isolated and characterized SBimide. When we spotted SBimide on the CASAD plates, we observed an orange annular pattern that differed from the orange disks obtained for SB or *epi*SB (Figure 6). The orange annulus bounded a concentric blue disk, the latter of which is where SBimide was positioned as a drop onto the plate. This pattern indicates that no iron was sequestered from the indicator where SBimide was spotted on the plate, but that iron was sequestered after SBimide diffused through the agar, resulting in formation of the orange ring.

We reasoned that *SBimide* converted to native SB as it diffused through the agar. To investigate this hypothesis, we incubated *SBimide* in aqueous buffer at pH 7.4 (10 mM HEPES) and analyzed the sample by mass spectrometry, and observed a change in  $m/z$  value from 430.1336 to 448.1442, which is consistent with ring opening of the imide and formation of SB (Figure S11C). Moreover, optical absorption spectroscopy revealed that *SBimide* only chelates Fe(III) under basic conditions whereas both SB and *epiSB* chelated Fe(III) at pH < 4 (Figure S6). In growth recovery assays with the  $\Delta sbnE$  and  $\Delta sirA$  mutants, *SBimide* provided siderophore activity comparable to that of SB (Figure S11A,B), which we attribute to its conversion to SB under these assay conditions. The fact that *SBimide* is ring-opened to generate SB under physiological conditions indicates that the presence of imide byproducts in the citric acid siderophore isolates from natural sources is most likely a consequence of the acid and base treatments employed during the isolation and purification steps, and that the imide is not physiologically relevant.

**Epimerization of the Citric Acid Stereocenter Perturbs Iron Sequestration from Transferrin.** Transferrin is the major Fe(III)-transport protein in serum, and the human protein binds Fe(III) with a  $pFe(III)$  value of 22.<sup>56</sup> Various studies have evaluated the ability of siderophores to sequester Fe(III) from transferrin,<sup>57,58</sup> and *S. aureus* can utilize holo-transferrin as an iron source.<sup>59-61</sup> Moreover, SB is reported to remove Fe(III) from holo-transferrin.<sup>60,61</sup> Transferrin has two lobes, and each lobe binds one equivalent of Fe(III) synergistically with carbonate. Urea PAGE affords separation of the four forms of transferrin – apo, holo (diferric), monoferric where Fe(III) is bound to the N-terminal lobe (mono-N transferrin), and monoferric where Fe(III) is bound to the C-terminal lobe (mono-C transferrin).<sup>62</sup> We used this technique to monitor the removal of Fe(III) from holo-transferrin by SB and *epiSB* (Figure 8). Following a 24-h incubation of holo-transferrin (40  $\mu$ M) with 10 to 50 equivalents of SB (50 mM Tris, 150 mM NaCl, 20 mM NaHCO<sub>3</sub>, pH 7.4, 37 °C), urea PAGE revealed a mixture of holo- and demetallated transferrin. Loss of Fe(III) from both the N- and C-terminal lobes occurred and the degree of Fe(III) removal was proportional to the SB concentration. At 30 and 50 equivalents of SB, bands

corresponding to apo-transferrin appeared, and these bands were absent from the control containing only holo-transferrin. Although *epiSB* was able to remove Fe(III) from holo-transferrin, as evidenced by the intensities of bands corresponding to the two monoferric transferrin species, *epiSB* sequestered markedly less Fe(III) from holo-transferrin than SB. We also monitored the holo-transferrin/siderophore mixtures over a 70-h time period by urea PAGE, and observed increased siderophore-dependent loss of Fe(III) from holo-transferrin over time (Figure S12). Under these experimental conditions, the kinetics of Fe(III) removal from holo-transferrin is relatively slow, even for SB. Nevertheless, the data support the notion that chirality at the citric acid stereocenter is important for the siderophore activity of SB.

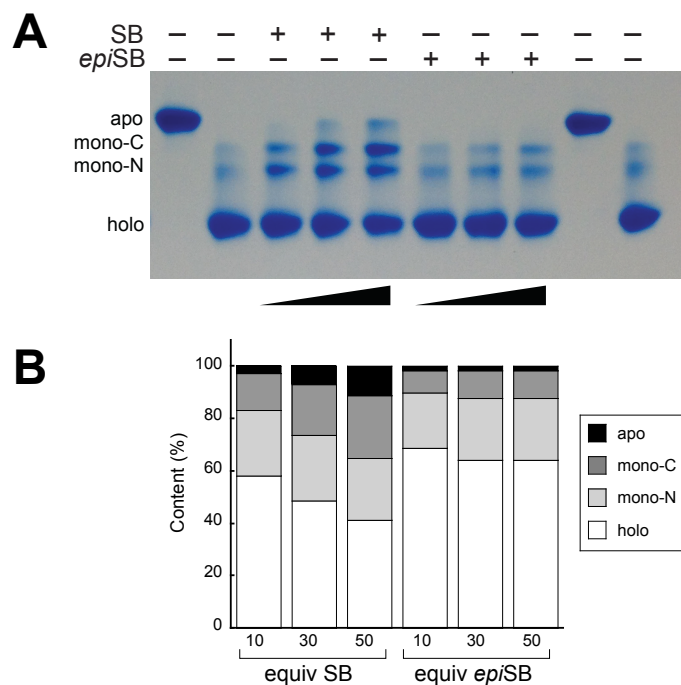


**Figure 8.** Siderophore-mediated iron sequestration from holo-transferrin monitored. (A) Holo-transferrin (40  $\mu$ M) was incubated with 0, 10, 30 or 50 equivalents of SB or *epiSB* and the solutions were incubated for 24 h at 37  $^{\circ}$ C in buffer. The resulting samples were analyzed by 6 M urea PAGE and Coomassie stain, and a representative gel is shown. (B) Quantification of the band intensities for the gel shown in A. Quantification was performed using ImageJ. Apo-transferrin, mono-C transferrin, mono-N transferrin and holo-transferrin are depicted in black, dark gray, light gray, and white, respectively.

## Summary

In this work, we report the first total synthesis of staphyloferrin B, a siderophore and virulence factor of *S. aureus*. The total synthesis along with computational modeling studies confirmed that SB exists as the hemiaminal form with an (*S*)-configuration of the citric acid moiety. Synthetic SB provided growth recovery of *S. aureus* that is dependent on its receptor SirA. The total synthesis provided a foundation for the preparation of two structural analogues, *epi*SB and *SBimide*. SB and *epi*SB differ only in the stereochemistry of the citric acid quaternary center. Fe(III)-binding studies and growth recovery assays provided valuable insight into the importance of the citric acid stereocenter for iron chelation and siderophore activity. Inversion of this stereocenter to generate *epi*SB alters the coordination sphere around the Fe(III) center and reduces the Fe(III) affinity relative to the native form. Although *epi*SB retains the ability to chelate iron and function as siderophore for *S. aureus in vitro*, the (*S*)-configuration at the citric acid moiety of SB appears to be important because the siderophore activity of *epi*SB is reduced in all contexts examined in this work. Our studies of *SBimide* confirmed that the imide ring is opened to generate the native siderophore SB under physiological conditions. In closing, *S. aureus* infections caused by recalcitrant and drug-resistant strains are a serious problem for public health. This work provides the necessary basis for further chemical and biological investigations of how SB contributes to the molecular pathogenesis of *S. aureus* infections as well as a guide for further synthetic efforts directed at achieving siderophore-based therapeutics for bacterial infections. Efforts along these lines are in progress.

## Acknowledgements

We thank the Pacific Southwest Research Center of Excellence, the Kinship Foundation (Sloan Foundation), and the Alfred Benzon Foundation (post-doctoral fellowship to J.L.H.M.) for financial support. We thank Toshiki Nakashige for purifying apo-transferrin and Prof. Timothy F. Jamison for use of an IR spectrometer. NMR instrumentation maintained by the MIT Department of Chemistry Instrumentation Facility (DCIF) is supported by NSF grants CHE-

9808061 and CHE-8915028. Circular dichroism instrumentation maintained by the MIT Biophysical Instrumentation Facility (BIF) is supported by NSF-0070319. The single-gene knockout transposon mutants were obtained from the Network on Antimicrobial Resistance in *Staphylococcus aureus* (NARSA) program distributing the Nebraska Transposon Mutant Library (NTML) of *S. aureus* mutants harboring single-gene knockouts, supported under NIAID/NIH contract no. HHSN272200700055C.

### Supporting Information

Experimental procedures, supporting tables, supporting figures, and spectroscopic data. This material is available free of charge via the Internet at <http://pubs.acs.org>.

### References

- (1) McGavin, M. J.; Heinrichs, D. E. *Front. Cell. Infect. Microbiol.* **2012**, *2*, 66.
- (2) DeDent, A.; Kim, H. K.; Missiakas, D.; Schneewind, O. *Semin. Immunopathol.* **2012**, *34*, 317-333.
- (3) Chambers, H. F.; DeLeo, F. R. Waves of resistance: *Nat. Rev. Microbiol.* **2009**, *7*, 629-641.
- (4) Cassat, J. E.; Skaar, E. P. *Cell Host Microbe* **2013**, *13*, 509-519.
- (5) Andrews, N. C.; Schmidt, P. J. *Annu. Rev. Physiol.* **2007**, *69*, 69-85.
- (6) Sheldon, J. R.; Heinrichs, D. E.. *FEMS Microbiol. Rev.* **2015**, ASAP.
- (7) Beasley, F. C.; Heinrichs, D. E. *J. Inorg. Biochem.* **2010**, *104*, 282-288.
- (8) Hammer, N. D.; Skaar, E. P. *Annu. Rev. Microbiol.* **2011**, *65*, 129-147.
- (9) Meiwes, J.; Fiedler, H.-P.; Haag, H.; Zähler, H.; Konetschny-Rapp, S.; Jung, G. *FEMS Microbiol. Lett.* **1990**, *67*, 201-205.
- (10) Sebulsky, M. T.; Heinrichs, D. E. *J. Bacteriol.* **2001**, *183*, 4994-5000.

- (11) Hider, R. C.; Kong, X. *Nat. Prod. Rep.* **2010**, *27*, 637-657.
- (12) Chu, B. C.; Garcia-Herrero, A.; Johanson, T. H.; Krewulak, K. D.; Lau, C. K.; Peacock, R. S.; Slavinskaya, Z.; Vogel, H. J. *Biomaterials* **2010**, *23*, 601-611.
- (13) Crosa, J. H.; Walsh, C. T. *Microbiol. Mol. Biol. Rev.* **2002**, *66*, 223-249.
- (14) Konetschny-Rapp, S.; Jung, G.; Meiwes, J.; Zähler, H. *Eur. J. Biochem.* **1990**, *191*, 65-74.
- (15) Drechsel, H.; Freund, S.; Nicholson, G.; Haag, H.; Jung, O.; Zähler, H.; Jung, G. *Biomaterials* **1993**, *6*, 185-192.
- (16) Haag, H.; Fiedler, H.-P.; Meiwes, J.; Drechsel, H.; Jung, G.; Zähler, H. *FEMS Microbiol. Lett.* **1994**, *115*, 125-130.
- (17) Mergeay, M.; Monchy, S.; Vallaëys, T.; Auquier, V.; Benotmane, A.; Bertin, P.; Taghavi, S.; Dunn, J.; van der Lelie, D.; Wattiez, R. *FEMS Microbiol. Rev.* **2003**, *27*, 385-410.
- (18) Janssen, P. J.; Van Houdt, R.; Moors, H.; Monsieurs, P.; Morin, N.; Michaux, A.; Benotmane, M. A.; Leys, N.; Vallaëys, T.; Lapidus, A.; Monchy, S.; Medigue, C.; Taghavi, S.; McCorkle, S.; Dunn, J.; van der Lelie, D.; Mergeay, M. *PLoS One* **2010**, *5*, e10433.
- (19) Gilis, A.; Khan, M. A.; Cornelis, P.; Meyer, J. M.; Mergeay, M.; van der Lelie, D. *J. Bacteriol.* **1996**, *178*, 5499-5507.
- (20) Münzinger, M.; Taraz, K.; Budzikiewicz, H. *Z. Naturforsch. C* **1999**, *54*, 867-875.
- (21) Grigg, J. C.; Cheung, J.; Heinrichs, D. E.; Murphy, M. E. P. *J. Biol. Chem.* **2010**, *285*, 34579-34588.
- (22) Dale, S. E.; Sebulsky, M. T.; Heinrichs, D. E. *J. Bacteriol.* **2004**, *186*, 8356-8362.
- (23) Bhatt, G.; Denny, T. P. *J. Bacteriol.* **2004**, *186*, 7896-7904.
- (24) Dale, S. E.; Doherty-Kirby, A.; Lajoie, G.; Heinrichs, D. E. *Infect. Immun.* **2004**, *72*, 29-37.
- (25) Cheung, J.; Beasley, F. C.; Liu, S.; Lajoie, G. A.; Heinrichs, D. E. *Mol. Microbiol.* **2009**, *74*, 594-608.

- (26) Beasley, F. C.; Cheung, J.; Heinrichs, D. E. *BMC Microbiol.* **2011**, *11*, 199.
- (27) Kobylarz, M. J.; Grigg, J. C.; Takayama, S.-i. J.; Rai, D. K.; Heinrichs, D. E.; Murphy, M. E. *Chem. Biol.* **2014**, *21*, 379-388.
- (28) Cheung, J.; Murphy, M. E. P.; Heinrichs, D. E. *Chem. Biol.* **2012**, *19*, 1568-1578.
- (29) Kobylarz, M. J.; Grigg, J. C.; Sheldon, J. R.; Heinrichs, D. E.; Murphy, M. E. P. *J. Biol. Chem.* **2014**, *289*, 33797-33807.
- (30) Hannauer, M.; Sheldon, J. R.; Heinrichs, D. E. *FEBS Lett.* **2015**, 730-737.
- (31) Challis, G. L. *ChemBioChem* **2005**, *6*, 601-611.
- (32) Sheldon, J. R.; Marolda, C. L.; Heinrichs, D. E. *Mol. Microbiol.* **2014**, *92*, 824-839.
- (33) Friedman, D. B.; Stauff, D. L.; Pishchany, G.; Whitwell, C. W.; Torres, V. J.; Skaar, E. P. *PLoS Pathog.* **2006**, *2*, e87.
- (34) Beasley, F. C.; Vinés, E. D.; Grigg, J. C.; Zheng, Q.; Liu, S.; Lajoie, G. A.; Murphy, M. E. P.; Heinrichs, D. E. *Mol. Microbiol.* **2009**, *72*, 947-963.
- (35) Lindsay, J. A.; Riley, T. V. *Infect. Immun.* **1994**, *62*, 2309-2314.
- (36) Lindsay, J. A.; Riley, T. V.; Mee, B. J. *Eur. J. Clin. Microbiol. Infect. Dis.* **1994**, *13*, 1063-1066.
- (37) Hanses, F.; Roux, C.; Dunman, P. M.; Salzberger, B.; Lee, J. C. *Genome Med.* **2014**, *6*, 93.
- (38) Tripathi, A.; Schofield, M. M.; Chlipala, G. E.; Schultz, P. J.; Yim, I.; Newmister, S. A.; Nusca, T. D.; Scaglione, J. B.; Hanna, P. C.; Tamayo-Castillo, G.; Sherman, D. H. *J. Am. Chem. Soc.* **2014**, *136*, 1579-1586.
- (39) Cancer Research Technology Limited. Patent. *WO2006/16143 A1* **2006**.
- (40) Seebach, D.; Naef, R.; Calderari, G. *Tetrahedron* **1984**, *40*, 1313-1324.
- (41) Eckelbarper, J. D.; Wilmot, J. T.; Epperson, M. T.; Thakur, C. S.; Shum, D.; Antczak, C.; Tarassishin, L.; Djaballah, H.; Gin, D. Y. *Chem. Eur. J.* **2008**, *14*, 4293-4306.
- (42) Carlsen, P. H. J.; Katsuki, T.; Martin, V. S.; Sharpless, K. B. *J. Org. Chem.* **1981**, *46*, 3936-3938.

- (43) Barbeau, K.; Zhang, G.; Live, D. H.; Butler, A. Petrobactin, a photoreactive siderophore produced by the oil-degrading marine bacterium *Marinobacter hydrocarbonoclasticus*. *J. Am. Chem. Soc.* **2002**, *124*, 378-379.
- (44) Küpper, F. C.; Carrano, C. J.; Kuhn, J.-U.; Butler, A. *Inorg. Chem.* **2006**, *45*, 6028-6033.
- (45) Shin, S. H.; Lim, Y.; Lee, S. E.; Yang, N. W.; Rhee, J. H. *J. Microbiol. Meth.* **2001**, *44*, 89-95.
- (46) Schwyn, B.; Neilands, J. B. *Anal. Biochem.* **1987**, *160*, 47-56.
- (47) Harris, W. R.; Carrano, C. J.; Raymond, K. N. *J. Am. Chem. Soc.* **1979**, *101*, 2722-2727.
- (48) Abergel, R. J.; Zawadzka, A. M.; Raymond, K. N. *J. Am. Chem. Soc.* **2008**, *130*, 2124-2125.
- (49) Bugdahn, N.; Oberthür, M. *Eur. J. Org. Chem.* **2014**, *2014*, 426-435.
- (50) Seyedsayamdost, M. R.; Traxler, M. F.; Zheng, S.-L.; Kolter, R.; Clardy, J. *J. Am. Chem. Soc.* **2011**, *133*, 11434-11437.
- (51) Connelly, N. G.; Damhus, T.; Hartshorn, R. M.; Hutton, A. T. *Nomenclature of inorganic chemistry. IUPAC recommendations 2005; Royal Society of Chemistry Publishing / IUPAC: Cambridge, UK 2005.*
- (52) Banerjee, S.; Ghosh, A.; Wu, B.; Lassahn, P.-G.; Janiak, C. *PPolyhedron* **2005**, *24*, 593-599.
- (53) Ozawa, T. C.; Kang, S. J.. *J. Appl. Crystallogr.* **2004**, *37*, 679.
- (54) Fey, P. D.; Endres, J. L.; Yajjala, V. K.; Widhelm, T. J.; Boissy, R. J.; Bose, J. L.; Bayles, K. W. *mBio* **2013**, *4*, e00537-00512.
- (55) Takeuchi, Y.; Nagao, Y.; Toma, K.; Yoshikawa, Y.; Akiyama, T.; Nishioka, H.; Abe, H.; Harayama, T.; Yamamoto, S. *Chem. Pharm. Bull.* **1999**, *47*, 1284-1287.
- (56) Martin, R. B.; Savory, J.; Brown, S.; Bertholf, R. L.; Wills, M. R. *Clin. Chem.* **1987**, *33*, 405-407.
- (57) Pollack, S.; Aisen, P.; Lasky, F. D.; Vanderhoff, G. *Br. J. Haematol.* **1976**, *34*, 231-235.

- (58) Ford, S.; Cooper, R. A.; Evans, R. W.; Hider, R. C.; Williams, P. H. *Eur. J. Biochem.* **1988**, *178*, 477-481.
- (59) Modun, B.; Evans, R. W.; Joannou, C. L.; Williams, P. *Infect. Immun.* **1998**, *66*, 3591-3596.
- (60) Park, R.-Y.; Sun, H.-Y.; Choi, M.-H.; Bai, Y.-H.; Shin, S.-H. *S. J. Microbiol.* **2005**, *43*, 183-190.
- (61) Beasley, F. C.; Marolda, C. L.; Cheung, J.; Buac, S.; Heinrichs, D. E. *S. Infect. Immun.* **2011**, *79*, 2345-2355.
- (62) Makey, D. G.; Seal, U. S. *Biochim. Biophys. Acta* **1976**, *453*, 250-256.

# TOC graphic

